Real-time x-ray scattering study of surface morphology evolution during ion erosion and epitaxial growth of Au(111)

M. V. Ramana Murty, T. Curcic, A. Judy, and B. H. Cooper
Department of Physics and Cornell Center for Materials Research, Cornell University, Ithaca, New York 14853

A. R. Woll and J. D. Brock
School of Applied and Engineering Physics and Cornell Center for Materials Research, Cornell University, Ithaca, New York 14853

S. Kycia and R. L. Headrick
Cornell High Energy Synchrotron Source (CHESS) and Cornell Center for Materials Research, Wilson Laboratory, Ithaca, New York 14853

(Received 11 February 1999)

We describe a detailed real-time x-ray scattering study of the evolution of the surface morphology of Au(111) both during ion erosion with 500-eV Ar^+ ions, and during homoepitaxial growth. We monitor the erosion and growth morphologies as a function of substrate temperature. We also monitor the surface reconstruction, since it is known to play an important role in determining growth regimes on Pt(111). Ion irradiation of Au(111) leads to surface morphology evolution by step retraction above 270 °C and quasi-layer-by-layer removal at 90–220 °C. The extent of the surface reconstruction on Au(111) during ion irradiation gradually decreases with decreasing temperature. While the herringbone reconstruction remains during ion irradiation at 270 °C, the long range order is lost and only the $(22\times\sqrt{3})$ reconstruction is present at 170 °C. We also observe layer-by-layer growth in the Au/Au(111) system at 55–145 °C, a result that differs from the usual behavior of homoepitaxy on fcc(111) surfaces. As in the layer-by-layer erosion regime, only the $(22\times\sqrt{3})$ reconstruction is present during layer-by-layer growth. Room temperature ion irradiation leads to a (1×1) surface structure and a three-dimensional rough morphology exhibiting pattern formation with a characteristic lateral length scale. Line-shape analysis of the diffuse scattering in transverse x-ray scans taken during low temperature ion irradiation, indicates that the characteristic lateral length scale increases with time consistent with a power law $l\sim t^{0.28}$. This agrees with a simple analysis of the position of the satellite peak in the diffuse scattering in these transverse x-ray scans. [S0163-1829(99)10647-7]

I. INTRODUCTION

Ion beam erosion of materials is commonly used for patterning in device fabrication and in thin film composition analysis techniques such as secondary ion mass spectrometry (SIMS). Ion beam irradiation at low temperatures can lead to a variety of surface morphologies including a self-affine surface,[1] a rippled surface,[2,3,4] and a patterned surface with mounds and pits.[5,6,7] The choice of the optimal irradiation conditions to minimize overetching during device fabrication or to improve depth resolution in SIMS, can be aided by a better understanding of the evolution of surface morphology during ion bombardment.

Control of the surface morphology at the monolayer scale requires an understanding of the relative importance of different microscopic mechanisms controlling mass flow during the erosion process. While considerable effort has been made to develop such an understanding for morphology evolution during epitaxial thin film growth, less is known about morphology evolution during ion erosion. In a simple view, ion erosion is the mirror image of epitaxy. In detail, this simple picture is complicated by the fact that ion erosion involves subsurface deposition of energy and both adatom and vacancy kinetics[8] are important for the determination of the surface morphology. Relevant questions to ask include: are the regimes of surface morphology evolution during ion erosion the same as those during epitaxy; and, can surface morphology evolution during ion erosion be described in terms of scaling laws developed for thin film growth?[9]

We present below the results of a study of both ion erosion and epitaxial growth on the (111) surface of Au. The (111) surfaces of fcc metals are interesting for a number of reasons. Thin films of Cu, Ag, and Au often serve as the nonmagnetic spacer material in magnetic multilayers. These films are often sputter deposited and exhibit a (111) texture[10] due to the low surface free energy of the (111) orientation. It is interesting that is there no layer-by-layer growth regime on single crystal fcc (111) metal surfaces such as Cu, Ag, and Ni.[11] As the substrate temperature is increased, a direct transition from three-dimensional rough growth to step flow growth is observed. This behavior is due to the large Ehrlich-Schwoebel barrier for adatoms in these systems.[11] The Pt(111) surface is an exception to this rule, exhibiting reentrant layer-by-layer growth.[12,13] The surface reconstruction on Pt(111) at high temperatures plays a crucial role in promoting the layer-by-layer growth at high temperatures (470–800 K).[14] Less is known about homoepitaxy on the Au(111) surface. A scanning tunneling microscopy (STM) study of Au(111) homoepitaxy indicated three-dimensional growth after 5 ML of deposition at room temperature.[15] Theoretical calculations based on effective medium theory suggest that there is a large Ehrlich-Schwoebel barrier for adatom diffu-

sion on Au(111), and that there should be no layer-by-layer growth regime.[16]

In this paper, we describe a detailed x-ray scattering investigation of the evolution of both the surface morphology and the surface reconstruction of Au(111) during 500-eV Ar^+ ion irradiation and during homoepitaxy. X-ray scattering is an ideal probe for monitoring the surface morphology and structure *in situ* and in *real time*, and can thus be used to determine the influence of substrate temperature, as well as growth and ion bombardment parameters. In a previous paper,[5] we reported the observation of changes in surface morphology evolution with decreasing temperature, from step retraction ($>270\,°C$), to layer-by-layer removal (120–220 °C), to rough erosion and pattern formation ($<60\,°C$) during 500-eV Ar^+ ion erosion of Au(111). Here we show a more complete data set taken during these erosion regimes, also showing the changes in the surface reconstruction with temperature. At high temperature ($\geqslant 270\,°C$) the surface shows the herringbone pattern, while in the layer-by-layer regime the surface exhibits only the $(22\times\sqrt{3})$ reconstruction. Room temperature ion irradiation leads to complete loss of the surface reconstruction. We also observe layer-by-layer growth during homoepitaxy on Au(111) at 55–145 °C, a result that differs from the usual behavior of homoepitaxy on fcc(111) surfaces.[11] During layer-by-layer growth, as in the layer-by-layer erosion regime, the herringbone reconstruction characteristic of Au(111) is lost, and the surface exhibits only the $(22\times\sqrt{3})$ reconstruction. Room temperature ion irradiation leads to pattern formation on Au(111). We show the results of a line-shape analysis of the diffuse scattering in transverse x-ray scans taken during low temperature ion irradiation. The analysis uses as input parameters the shape, size, and position distributions of the features in the pattern. The scaling exponent for the variation of the spacing between features with time obtained from the line-shape analysis agrees with our more simple analysis reported earlier[5] and also agrees with a continuum model for molecular beam epitaxy.[17]

The paper is organized as follows. In Sec. II we describe the details of the experimental apparatus and the x-ray scattering geometry. Scattering from a clean, reconstructed Au(111) surface is described in Sec. III. We discuss in Sec. IV the evolution of surface morphology and surface reconstruction during ion irradiation, and in Sec. V the same during homoepitaxy. In Sec. VI we describe pattern formation on Au(111) during low temperature ion irradiation. In Sec. VII we discuss x-ray line-shape analysis and in Sec. VIII we summarize the main results.

II. EXPERIMENT

X-ray scattering experiments were performed on the A2 line at the Cornell High Energy Synchrotron Source (CHESS). X rays from the synchrotron pass through a double bounce monochromator before entering the ultrahigh vacuum chamber (UHV). The energy E of the x rays was chosen to be 10 keV (wavelength $\lambda=1.24$ Å) or 11 keV ($\lambda=1.13$ Å). The monochromator was either a pair of W/B_4C multilayers with a bandpass $\Delta E/E\approx 0.01$, or a pair of Si(111) crystals with $\Delta E/E\approx 0.0004$. A grazing incidence mirror (*Rh*) was placed after the double bounce monochromator to eliminate third and higher harmonics from the incident beam when using the Si(111) crystals. The scattered x-ray intensity from the Au(111) sample was measured using a NaI(T1) scintillation detector.

The details of the x-ray scattering geometry are described elsewhere.[18] The UHV chamber is mounted on a four circle diffractometer that permits independent variation of the incident angle α, the outgoing scattering angle β, the transverse scattering angle Δ and the sample azimuth ϕ. The magnitude and direction of the scattered wave vector $\mathbf{q}\equiv(q_\parallel,q_z)=\mathbf{k}_0-\mathbf{k}$ determines the type of information that can be obtained from x-ray scattering. Here, $\mathbf{k}_0$ and $\mathbf{k}$ are the incident and scattered wave vectors, and $q_\parallel$ and q_z refer to the components of $\mathbf{q}$ parallel and perpendicular to the (111) surface, respectively. Measurement of the specular beam intensity ($q_\parallel=0$) gives information about surface roughness in the direction normal to the surface. Off-specular diffuse scattering ($q_\parallel\neq 0$) gives information about lateral correlations in the surface morphology.

The base pressure in the UHV chamber was 3×10^{-10} mbar. A Au(111) single crystal with a miscut of less than 0.1° was used for the experiments. The smooth starting surface was prepared by repeated sputtering and annealing cycles at 350–450 °C. Auger electron spectroscopy did not show any contaminants, indicating that impurity levels were below $\approx$ 0.1% of a ML. The sample temperature was measured using a thermocouple connected to the substrate holder. The thermocouple was calibrated against a pyrometer in the temperature range 80–200 °C. Temperatures outside this range were obtained from an extrapolation of the thermocouple-pyrometer calibration curve. Sputter erosion experiments were performed with 500-eV Ar^+ ions, incident at 45° with respect to the surface normal. The chamber was filled with Ar to a pressure of 5×10^{-5} mbar during sputtering. An effusion cell was used for Au homoepitaxy.

III. DIFFRACTION FROM CLEAN, RECONSTRUCTED Au(111)

In this section, we discuss the x-ray scattering observed from a clean, smooth, and reconstructed Au(111) surface. Bulk Au(111) has the fcc structure with a lattice constant $a=4.08$ Å in the conventional simple cubic unit cell representation. On the surface, atoms rearrange themselves into $22\times\sqrt{3}$ cells with 23 atoms squeezed into 22 sites. Due to the threefold symmetry about the (111) axis, there exist three equivalent $(22\times\sqrt{3})$ domains that, in turn, arrange to form a herringbone pattern. The surface reconstruction of Au(111) has been studied previously using low energy electron diffraction (LEED),[19] helium atom scattering,[20] STM,[21,22] and x-ray scattering.[23]

In describing the x-ray scattering geometry, the reciprocal space directions $(H\,K\,L)_{\rm hex}$ will be written in the hexagonal notation (subscript hex).[23] Real-space directions will be given in the conventional simple cubic unit cell notation (subscript cubic). The real-space basis vectors in the simple

cubic unit cell representation are

$$\mathbf{a}_1 = a\hat{\mathbf{x}},$$

$$\mathbf{a}_2 = a\hat{\mathbf{y}},$$

$$\mathbf{a}_3 = a\hat{\mathbf{z}}. \quad (1)$$

In the hexagonal notation, the real-space basis vectors are taken as

$$\mathbf{A}_1 = \frac{a}{2}(-\hat{\mathbf{x}}+\hat{\mathbf{y}}),$$

$$\mathbf{A}_2 = \frac{a}{2}(-\hat{\mathbf{y}}+\hat{\mathbf{z}}),$$

$$\mathbf{A}_3 = a(\hat{\mathbf{x}}+\hat{\mathbf{y}}+\hat{\mathbf{z}}), \quad (2)$$

giving the reciprocal space basis vectors

$$\mathbf{B}_1 = \frac{4\pi}{3a}(-2\hat{\mathbf{x}}+\hat{\mathbf{y}}+\hat{\mathbf{z}}),$$

$$\mathbf{B}_2 = \frac{4\pi}{3a}(-\hat{\mathbf{x}}-\hat{\mathbf{y}}+2\hat{\mathbf{z}}),$$

$$\mathbf{B}_3 = \frac{2\pi}{3a}(\hat{\mathbf{x}}+\hat{\mathbf{y}}+\hat{\mathbf{z}}). \quad (3)$$

Figure 1(a) shows a schematic of a constant L plane of the reciprocal space and Figs. 1(b) and 1(c) show the section near the $(10)_{\text{hex}}$ truncation rod for a reconstructed Au(111) surface. Note that all reconstruction spots are not shown in Figs. 1(b) and 1(c) for the sake of clarity. A surface with the three rotationally equivalent $(22\times\sqrt{3})$ domains but no herringbone pattern will have a diffraction pattern, as shown in Fig. 1(b) with $\delta_D = 2\sqrt{2}\pi/22a = 0.099\ \text{Å}^{-1}$. With a herringbone pattern, the diffraction pattern would appear as in Fig. 1(c). Note that the reciprocal space spots due to the $(22\times\sqrt{3})$ unit cell are not present when the surface is fully covered by the herringbone pattern.

A sketch of the LEED pattern from a clean, reconstructed Au(111) surface (observed in a separate vacuum chamber) is overlaid on the constant L plane in Fig. 1(a). Only the short range order ($22\times\sqrt{3}$ unit cell) is seen in LEED due to the small coherence length of our instrument. Figure 1(c) is a $(1.034-q^*/\sqrt{3}, 2q^*/\sqrt{3}, 0.08)_{\text{hex}}$ x-ray scan, indicated by the dashed line in Fig. 1(c), showing the herringbone pattern on the surface. The separation between the peaks $\delta_K \approx 0.026\ \text{Å}^{-1}$ corresponds to a surface unit cell dimension of 242 Å along the $\langle 110\rangle_{\text{cubic}}$ direction, in close agreement with a previous STM study (250 Å).[22]

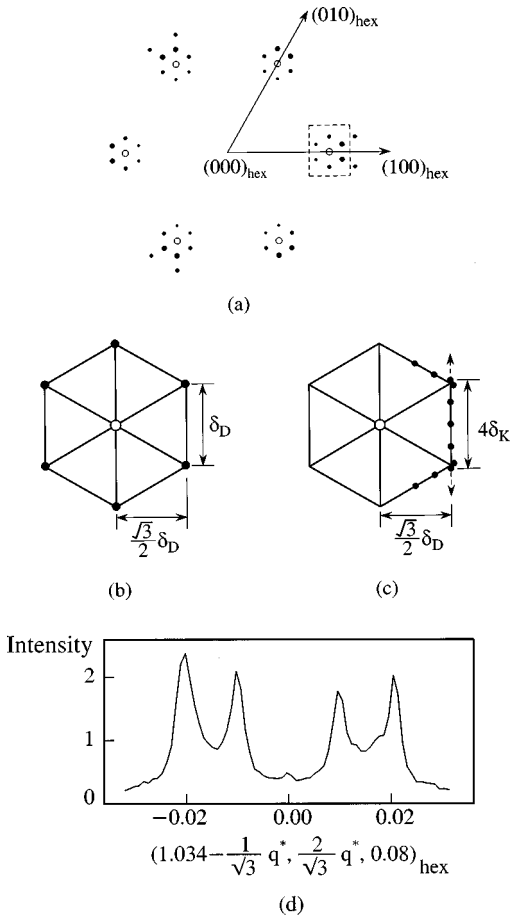

FIG. 1. (a) The reciprocal lattice with directions in the hexagonal notation for the Au(111) surface. The low energy electron diffraction pattern observed from the clean, reconstructed Au(111) is also sketched. The bulk spots are shown as open circles and the surface reconstruction spots as solid circles. The LEED pattern is not drawn to scale. (The region around the $\{10\}_{\text{hex}}$ rods is enlarged for clarity.) (b) and (c) show expanded views of the region around the $(10)_{\text{hex}}$ truncation rod, indicated by the dashed box in (a), for the Au(111) surface; (b) corresponds to the $(22\times\sqrt{3})$ reconstruction; and (c) the herringbone pattern. Note that the spots due to $(22\times\sqrt{3})$ reconstruction are not present on a surface with the herringbone pattern. (d) A $(1.034-q^*/\sqrt{3}, 2q^*/\sqrt{3}, 0.08)_{\text{hex}}$ x-ray scan from the clean, reconstructed Au(111) surface showing the herringbone pattern. The direction of the scan is indicated by the dashed line in (c). The separation between two adjacent peaks corresponds to a unit cell dimension of 242 Å.

IV. SURFACE RECONSTRUCTION OF Au(111) DURING ION IRRADIATION

In this section, we discuss a real-time x-ray scattering investigation of the evolution of both the surface morphology and the surface reconstruction on Au(111) during ion irradiation. Figure 2 shows the evolution of the specular beam intensity at the $(0\ 0\ 1.44)_{\text{hex}}$ position, close to the anti-Bragg $(0\ 0\ 1.5)_{\text{hex}}$ position,[24] during 500-eV Ar^+ ion irradiation at various substrate temperatures in the range 35–270 °C. In this geometry, the x rays scattered from two successive (111) planes in the crystal are approximately 180° (more precisely 173°) out-of-phase, maximizing sensitivity to changes in the surface roughness.[25] The nearly constant specular beam intensity at 270 °C indicates surface evolution by step retraction. The loss of specular beam intensity at 35 °C indicates the development of three-dimensional roughness. At intermediate temperatures of 120–220 °C we see intensity oscillations indicating quasi-layer-by-layer removal. Quasi-layer-by-layer sputtering has been previously observed on Si(100),[26] and Si(111),[27] using reflection high-

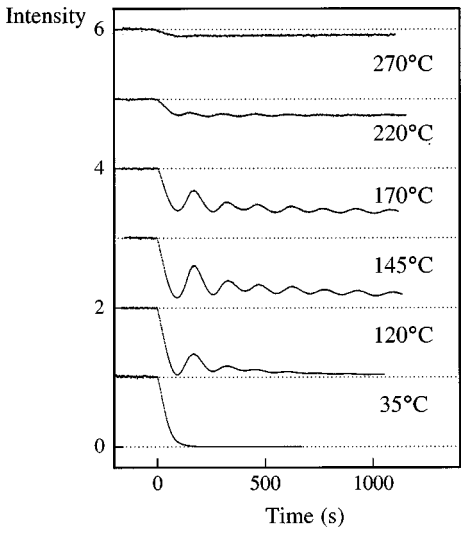

FIG. 2. Evolution of the specular beam intensity at the $(0\ 0\ 1.44)_{hex}$ position during 500-eV Ar^+ irradiation. The evolution of the intensity at different temperatures is offset vertically for clarity.

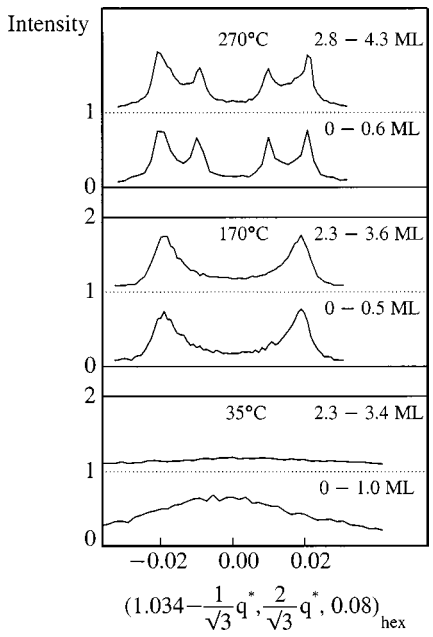

FIG. 3. X-ray scans taken during 500-eV Ar^+ ion irradiation at different substrate temperatures and at different times during erosion. The $(1.034-q^*/\sqrt{3},2q^*/\sqrt{3},0.08)_{hex}$ scans show the variation of the surface reconstruction during ion erosion. (a) 270 °C, the herringbone pattern is maintained during ion irradiation; (b) 120 °C, only the short range order is retained with $(s\times\sqrt{3})$ reconstruction, $s=22-23$; and (c) 35 °C, the surface reverts to a (1×1) structure. The x-ray scans were taken during ion irradiation with the start and end coverages indicated.

energy electron diffraction, and on Pt(111),[28] using helium atom scattering. Previous STM studies of ion irradiated Au(111) have also suggested a layer-by-layer sputtering regime.[29,30]

Since surface reconstruction can play a crucial role in surface morphology evolution (Ref. 14 and see below), we investigated the evolution of the surface reconstruction during ion irradiation. Figure 3 shows $(1.034-q^*/\sqrt{3},2q^*/\sqrt{3},0.08)_{hex}$ scans [dashed line in Fig. 1(c)] taken through the surface reconstruction peaks during 500-eV Ar^+ ion irradiation at different substrate temperatures. Comparing with Figs. 1(c) and 1(d), we see that the herringbone pattern is retained *during* ion erosion in the step retraction regime at 270 °C. However, the intensities of the peaks are about 30% less than those obtained from the clean surface [Fig. 1(d)], indicating some amount of disorder in the arrangement of the $22\times\sqrt{3}$ domains. In the quasi-layer-by-layer sputtering regime at 170 °C, the long range order (herringbone pattern) is lost. However, the $(s\times\sqrt{3})$ motif, $s=22-23$, is still present [compare with Fig. 1(b)]. At 35 °C, both the long and short range order are lost and the surface reverts to a (1×1) structure.

The different regimes of surface morphology evolution during ion erosion of Au(111) are analogous to those commonly observed during molecular beam epitaxy. The extent of the surface reconstruction on Au(111) during ion irradiation gradually decreases with decreasing temperature.

V. Au/Au(111) HOMOEPITAXY

Since we observe a layer-by-layer sputtering regime on Au(111), what about the inverse process of Au/Au(111) homoepitaxy? On fcc(111) metal surfaces such as Cu, Ag, and Ni, there is no layer-by-layer growth regime and a direct transition from three-dimensional growth to step flow growth is observed with increasing temperature.[11]

Figure 4(a) shows the variation of the specular beam intensity at the $(0\ 0\ 1.44)_{hex}$ position [near the anti-Bragg position $(0\ 0\ 1.5)_{hex}$] during deposition of Au on Au(111). Intensity oscillations were observed in the temperature range 55–145 °C. The oscillations have the parabolic shape indicating close to ideal layer-by-layer growth. Figure 4(b) shows a $(1.034-q^*/\sqrt{3},2q^*/\sqrt{3},0.08)_{hex}$ scan taken after deposition of 0.1 ML at 70 °C. The surface has the $(22\times\sqrt{3})$ reconstruction. Scans taken both during and after deposition of 4 ML indicate that the surface has the $(22\times\sqrt{3})$ reconstruction during growth at 70 °C. The herringbone pattern is lost within 0.1 ML after deposition has begun.

A previous STM study of Au/Au(111) epitaxy reported three-dimensional growth after 5 ML of deposition at room temperature.[15] However, snapshots of the surface at different film thicknesses reported in Ref. 15 are consistent with there being a few specular beam intensity oscillations had they used a diffraction probe.[31] As noted above, the observation of quasi-layer-by-layer growth in Au(111) homoepitaxy is in contrast to the other fcc transition metals Cu, Ag, and Ni.[11,32] A high Ehrlich-Schwoebel barrier for adatoms in the Cu/Cu(111) and Ag/Ag(111) systems is responsible for the absence of the layer-by-layer growth regime. In fact, atomistic calculations also suggested a high Ehrlich-Schwoebel barrier for adatoms on Au/Au(111) and that the layer-by-layer regime should not occur on Au/Au(111).[16]

One explanation for the observation of layer-by-layer growth is that Au adatoms face a small Ehrlich-Schwoebel barrier. Alternately, the mechanism for layer-by-layer growth on Au(111) may be similar to the one responsible for the high temperature (470–800 K) layer-by-layer growth observed in Pt/Pt(111).[12,14] In contrast to the (111) surfaces of

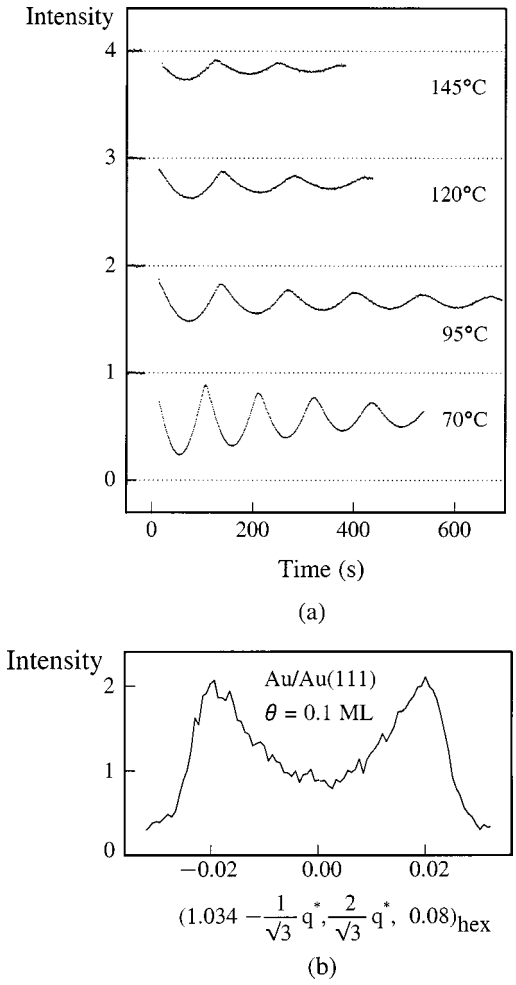

FIG. 4. Evolution of the specular beam intensity at the $(0\ 0\ 1.44)_{hex}$ position during Au(111) homoepitaxy. The evolution of the intensity at different temperatures is offset vertically for clarity.

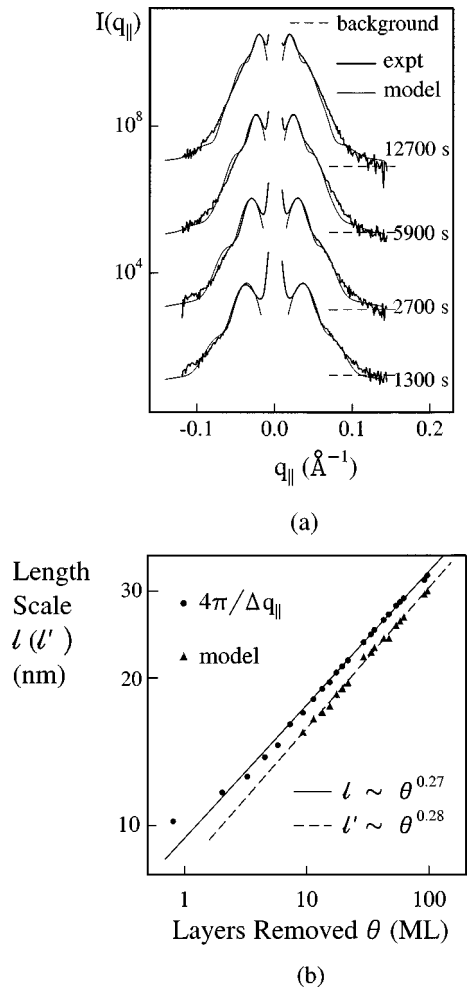

FIG. 5. (a) Low angle transverse x-ray scans (dark lines) through $(0\ 0\ 0.15)_{hex}$ taken during 500-eV Ar^+ ion irradiation at 35 °C. Only the diffuse scattering is shown. The scans are offset vertically for clarity. The light lines are fits to the experimentally observed line shapes using the model described in Sec. VII. The parameters in the model are (i) at 1300 s, $\phi = 12°$, $2R = 155$ Å, $\sigma_1 = 17$ Å, $\sigma_2 = 0.2$; (ii) at 2700 s, $\phi = 12°$, $2R = 190$ Å, $\sigma_1 = 17$ Å, $\sigma_2 = 0.2$; (iii) at 5900 s, $\phi = 13°$, $2R = 240$ Å, $\sigma_1 = 22$ Å, $\sigma_2 = 0.2$; and (iv) at 12700 s, $\phi = 14°$, $2R = 295$ Å, $\sigma_1 = 25$ Å, $\sigma_2 = 0.2$. (b) The variation of the average separation of features with the number of monolayers removed. The scaling exponent from the simple estimate made from the position of the satellite peak l agrees with the more detailed model (l' in Sec. VII).

Cu, Ag, and Ni that do not reconstruct, the Au(111) surface undergoes a reconstruction to form a herringbone pattern (or just the $(22\times\sqrt{3})$ reconstruction). At high temperatures, Pt(111) has a reconstruction similar to that on Au(111).[14] In Pt/Pt(111) epitaxy, adatoms diffuse slowly on the reconstructed Pt(111) surface (resulting in a high island nucleation density) but diffuse rapidly on top of the unreconstructed islands.[14] Thus island coalescence sets in before the island size gets close to the critical radius for second layer nucleation, resulting in layer-by-layer growth.[33]

VI. LOW TEMPERATURE ION IRRADIATION: PATTERN FORMATION

We now turn our attention to ion erosion at low temperatures. Ion irradiation at 35 °C leads to three-dimensional roughness as indicated by the loss of the specular beam intensity in Fig. 2. Transverse scans through the $(0\ 0)_{hex}$ truncation rod with $q_z = 0.133$ Å^{-1} ($L = 0.15$ in hexagonal units), taken during sputtering, are shown in Fig. 5(a). Satellite peaks in the diffuse scattering, located symmetrically about the specular position ($q_\parallel = 0$), are observed and indicate the development of features with a characteristic lateral length scale on the surface. The length scale is proportional to the average separation between features, assumed to be close packed. Determination of the average distance between features from the measured line shapes is complicated by the fact that the scattered x-ray intensity is influenced by the feature size and shape. We discuss a line-shape analysis in the next section. Here we make a simple estimate of how the characteristic length scale $l \approx 4\pi/\Delta q_\parallel$ varies with time, where $\Delta q_\parallel$ is the separation between the symmetrically placed satellite peaks. The variation of the length scale l with the amount of material removed (proportional to time) is shown in Fig. 5(b). The length scale increases with time, consistent with a power law $l \sim t^n$, where $n = 0.27 \pm 0.02$. A simple analysis of the line shapes, described in a previous paper,[5] also suggested that the aspect ratio of the features remains

nearly constant during ion irradiation.

The observation of pattern formation during ion irradiation suggests a diffusion bias for surface defects (vacancies/adatoms).[34] The diffusion of surface defects on both the terraces and along step edges can give rise to a diffusion bias. For diffusion on the terrace, an Ehrlich-Schwoebel barrier (activation barrier to joining a step from the upper terrace in excess of the terrace diffusion barrier) or a vacancy-step attraction[35] are possible sources of diffusion bias. Edge diffusion also generates a diffusion bias since the motion of defects along a step edge is, on average, directed toward the inner corners (''uphill'').[36] Continuum equations incorporating a diffusion bias[37,17] show pattern formation with the surface morphology consisting of mounds and pits. The length scale (proportional to the spacing between features) increases with time as neighboring mounds (and similarly pits) coalesce. The observation of a nearly constant aspect ratio of the features during their evolution[5] on Au(111) suggests slope selection along the sides of mounds and pits. Pattern formation of this nature with slope selection has been observed in molecular beam epitaxy.[38,39,40] The stable slope selected is the slope m where the diffusion bias current j_s vanishes and $\partial j_s/\partial m<0$.[37] The observed scaling exponent for the variation of the length scale with time, $n=0.27\pm0.02$, is close to the predicted value of 0.25 in a continuum model for surface morphology evolution during epitaxy.[5,17]

VII. LINE-SHAPE ANALYSIS

In this section we show that the scaling exponent obtained by tracking the positions of the satellite peaks (see above) is the same as that for the increase of the average separation between features with time, extracted using a model of the surface morphology that makes reasonable assumptions (see below). Consider the surface of area A to be completely covered by N features. The intensity for scattering from this surface is assumed to have the same general form as that for a dense gas or liquid,[41,42]

$$I(\mathbf{q})\propto N|F(\mathbf{q})|^2S(\mathbf{q}), \tag{4}$$

where $F(\mathbf{q})$ is the form factor of the feature and $S(\mathbf{q})$ is the structure factor. The structure factor $S(\mathbf{q})$ is related to the radial distribution function $g(\mathbf{r})$ of the features by[41]

$$S(\mathbf{q})-1=\frac{N}{A}\int d^2\mathbf{r}[g(\mathbf{r})-1]\exp(i\mathbf{q}\cdot\mathbf{r}). \tag{5}$$

Since the surface is covered by features of different sizes, we replace the square of the form factor in Eq. (4) by an average $\langle|F(\mathbf{q})|^2\rangle$ over a size distribution function $f(r)$. Since the average separation between features is small compared to the mean terrace size on the vicinal surface, it is reasonable to assume that the centers of features lie in a plane. This makes the structure factor independent of q_z.

The form factor of the features is peaked at $q_\parallel=0$ and is a decreasing function of $q_\parallel$ for small $q_\parallel$. On the other hand, the structure factor $S(q_\parallel)$ is an increasing function for small $q_\parallel$. Hence, the first peak in the intensity $I(q)$ would be expected to lie at a value of $q_\parallel=q_\parallel^0$ that is smaller than that corresponding to the first peak in $S(q_\parallel)$. The first peak in the structure factor $S(q_\parallel)$ is located close to $2\pi/l'$, where l' is the location of the first peak in the radial distribution function. Therefore, the value $2\pi/q_\parallel^0$ overestimates the average separation between features. For close-packed features of average radius R, both the width of the form factor and the location of the first peak in the structure factor will scale as R^{-1}. Since the intensity is a product of the form factor and the structure factor, the position of the satellite peak is also expected to scale as R^{-1} if the following assumptions are satisfied: (a) the size distribution function $f(r)$ of the features remains invariant; (b) the shape of the structure factor is invariant; and (c) the instrument resolution function is ideal (δ function). If these assumptions are satisfied, the scaling exponent obtained by tracking the positions of the satellite peaks will be the same as the scaling exponent for the evolution of length scale with time.

In order to estimate the scaling exponent, we now consider a simple model with a feature shape, a size distribution, and a structure factor. The surface created by ion erosion consists of features whose average size increases with time. In addition, the aspect ratio of the features stays relatively constant over time, indicating slope selection along the sides of the features.[5] This suggests that we take the feature shape to be conical with a base of diameter d and half angle $\pi/2-\phi$ [i.e., the tilt from the (111) orientation is ϕ]. Although previous LEED (Ref. 5) and STM (Ref. 29) studies indicated that steps on the sputtered surface run preferentially along $\langle 110\rangle$ directions, we ignore any azimuthal dependence in this simple model. The form factor is given by

$$F(q_\parallel,q_z)=\frac{2\pi}{q_z}\int_0^{d/2}J_0(q_\parallel r)\times r[\exp(iq_z(r-d/2)\tan\phi)-1]dr. \tag{6}$$

The size distribution function $f(r)$ is taken to be a Gaussian distribution with mean R (radius of base of the cone) and standard deviation σ_1.

We construct the structure factor $S(q)$ based on a tight-packed arrangement of circular disks on a hexagonal lattice. If the diameter of the disk is D, the nearest neighbors would lie at $D,\sqrt{3}D,2D,\sqrt{7}D,3D,\ldots$ with multiplicities 6, 6, 6, 12, 6, ... Since the reciprocal lattice of a hexagonal lattice is also a hexagonal lattice (except for a rotation of 30°), $S(q)$ would consist of a series of δ functions. We construct the structure factor for the ion-eroded surface by broadening the $S(q)$ of an ideal hexagonal lattice:

$$S(q_\parallel)=\sum_{i=1}^{n}\frac{1}{2\pi q_\parallel}\frac{a_i}{\sigma_2\sqrt{2\pi b_i}}\exp[-(q_\parallel-b_i)^2/2b_i\sigma_2^2]. \tag{7}$$

Here, b_i is the distance in reciprocal space to the ith nearest neighbor, and a_i is the multiplicity of the ith nearest neighbor. Two aspects to note about the form of $S(q)$ are (a) the peak corresponding to the ith nearest neighbor at $q_\parallel=b_i$ is broadened by a Gaussian function with variance $b_i\sigma_2^2$, and (b) the function $S(q)$ is taken to be cylindrically symmetrical and independent of q_z.

Finally, the experimentally measured intensity is a convolution of the calculated intensity, Eq. (4), with an instrument resolution function. A Gaussian function with standard de-

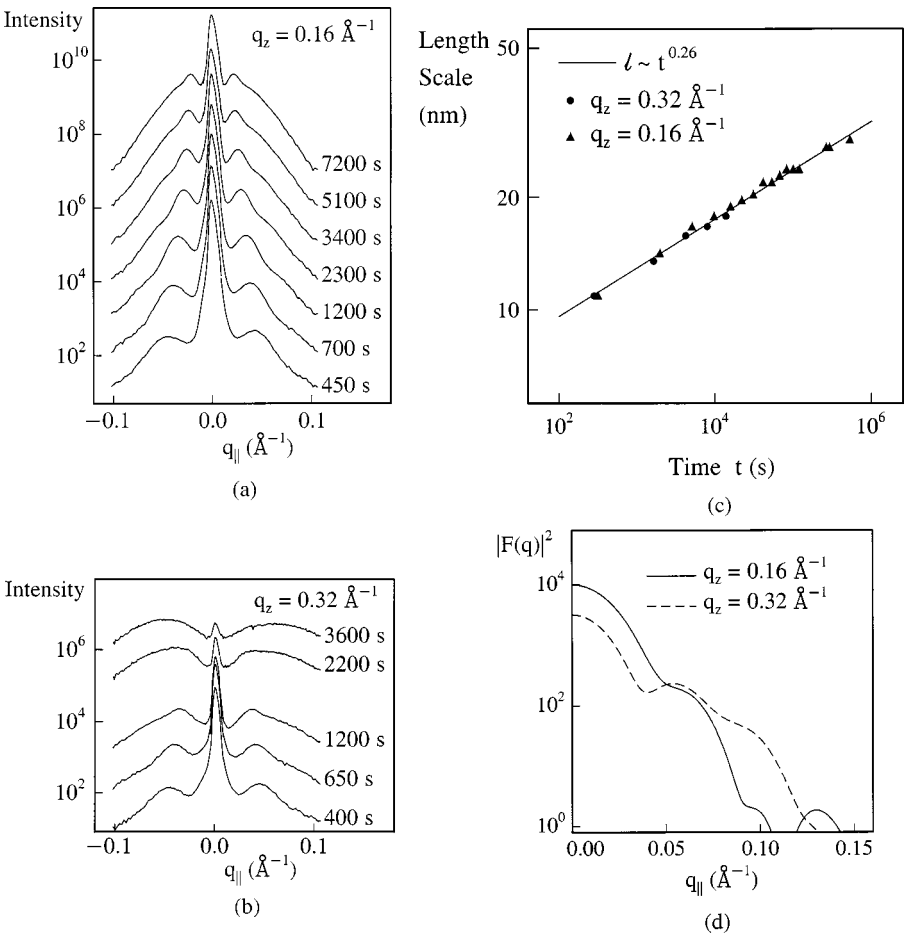

FIG. 6. Transverse x-ray scans through (a) $(0\,0\,0.18)_{\text{hex}}$, $q_z = 0.16\,\text{Å}^{-1}$, and (b) $(0\,0\,0.36)_{\text{hex}}$, $q_z = 0.32\,\text{Å}^{-1}$, taken during ion erosion at a rate of 210 ML/s with 500-eV Ar^+ ions at 35 °C. (c) The average separation between features l estimated from the position of the satellite peak in (a) and (b). (d) The square of the form factor $|F(q)|^2$ for a cone of radius $R = 100$ Å and angle $\phi = 12°$ at $q_z = 0.16\,\text{Å}^{-1}$ and 0.32 Å^{-1}.

viation of 0.0025 Å^{-1} gave a reasonable fit over two orders of magnitude to the measured intensity from the clean, starting surface and is taken as the instrument resolution function. (With a narrow incident beam spot size and detector window, peak widths as narrow as 0.001 Å^{-1} have been measured suggesting that the sample contributes little to the broadening of the specular beam).

The calculated line shapes are overlaid on the experimental data in Fig. 5(a). A constant intensity indicated by the dashed lines in Fig. 5(a) was added to the calculated intensity to account for the background counts. This analysis produced nearly constant values of σ_1/R, ϕ and σ_2 during the course of removing 10–100 ML, satisfying the assumptions of the heuristic argument presented above. The average separation between features l' is given by the first peak in the radial distribution function $g(r)$, calculated from the structure factor $S(q)$ using Eq. (5). Figure 5(b) shows a comparison of the length scale l' obtained from the line-shape analysis with the length scale l obtained from the simple estimate described in the previous section. While the absolute values of the length scale differ by ≈10%, the scaling exponents from the simple analysis and the more detailed line-shape analysis are close.

Finally, we note that the observation of the satellite peak and its association with an average distance between features on the surface can be done unambiguously only for transverse scans at low values of q_z.[43] Figures 6(a) and 6(b) show transverse scans through the $(0\,0)_{\text{hex}}$ truncation rod taken during sputtering at $q_z = 0.16\,\text{Å}^{-1}$ $(L = 0.18)$ and $0.32\,\text{Å}^{-1}(L = 0.36)$, respectively. The sputter rate was 210 s/ML in both experiments. A satellite peak is observed in the initial stages of sputtering at both values of q_z. Furthermore, the length scale estimated from the location of the satellite peak at both q_z is consistent at short times (<1000 s) as shown in Fig. 6(c); the satellite peak moves to smaller $|q_\parallel|$ with time indicating an increasing separation between features on the surface. At $q_z = 0.16\,\text{Å}^{-1}$, the satellite peak increases in intensity and moves to lower $|q_\parallel|$ throughout the 7200 s of sputtering. On the other hand, at $q_z = 0.32\,\text{Å}^{-1}$, the satellite peak gradually diminishes in intensity, becomes broader and moves to larger $|q_\parallel|$ after ≈1200 s. This, however, does not indicate a loss of order on the surface, since Fig. 6(a) clearly demonstrates the existence of a characteristic length scale up to long times.

The broadening of the satellite peak at the larger q_z can be understood from Eq. (4). Since the structure factor is independent of q_z, the broadening of the feature form factor with increasing q_z is responsible for the observation. As an illustration, Fig. 6(d) shows the square of the form factor $|F(q)|^2$ for a cone with a radius $R = 100$ Å and angle $\phi = 12°$ at $q_z = 0.16\,\text{Å}^{-1}$ and 0.32 Å^{-1}. Why does the form factor broaden with increasing q_z ? A simple picture is as follows. When the depth of surface corrugation exceeds $2\pi/q_z$, a point on the surface at $(x,y,z+2\pi/q_z)$ can be shifted to (x,y,z) without any change in the x-ray signal. The folding introduces lateral correlations at shorter length scales resulting in a broadening of the satellite peak. This can be seen in Fig. 6(d) where the scattering from a point at the base of the cone and at the tip of the cone is $q_z R \tan\phi = 1.08\pi$, and 2.16π out of phase at $q_z = 0.16\,\text{Å}^{-1}$ and 0.32 Å^{-1}, respectively.

VIII. CONCLUSION

We have reported a detailed x-ray scattering investigation of the evolution of the surface morphology and the surface reconstruction on Au(111) during 500-eV Ar^+ ion irradiation and homoepitaxy. Ion irradiation leads to the different regimes of step retraction (>270 °C), quasi-layer-by-layer removal (120–220 °C), and three-dimensional rough erosion (20–60 °C), analogous to the regimes commonly observed in molecular beam epitaxy. The extent of the surface reconstruction on Au(111) during ion irradiation gradually decreases with decreasing temperature. The herringbone pattern on Au(111) is retained in the step retraction regime at 270 °C, whereas the surface reverts to the unreconstructed (1×1) structure during pattern formation at 35 °C. During layer-by-layer erosion, the long range order is lost and the surface has only the $(22\times\sqrt{3})$ reconstruction. We also observe layer-by-layer growth in Au(111) homoepitaxy in the temperature range 55–145 °C. The surface has only the $(22\times\sqrt{3})$ reconstruction during homoepitaxy. Room temperature ion irradiation leads to pattern formation on Au(111). A line-shape analysis of the diffuse scattering from the patterned surface indicates that the average spacing between features increases with time, consistent with a power law $l \sim t^{0.28}$, in agreement with a simple analysis based on the position of the satellite peak in transverse x-ray scans. The scaling exponent is close to the predicted value of 0.25 in a continuum model for molecular beam epitaxy.[17]

ACKNOWLEDGMENTS

This work made use of the Cornell Center for Materials Research facilities supported by NSF under Grant No. DMR-9632275. Additional support was provided by AFOSR under Grant No. F49620-97-1-0020. Part of this work was conducted at CHESS, which is supported by the NSF under Grant No. DMR-9311772.

[1] E. A. Eklund, R. Bruinsma, J. Rudnick, and R. S. Williams, Phys. Rev. Lett. **67**, 1759 (1991).
[2] E. Chason, T. M. Mayer, B. K. Kellerman, D. T. McIlroy, and A. J. Howard, Phys. Rev. Lett. **72**, 3040 (1994).
[3] T. M. Mayer, E. Chason, and A. J. Howard, J. Appl. Phys. **76**, 1633 (1994).
[4] S. Rusponi, G. Costatini, C. Boragno, and U. Valbusa, Phys. Rev. Lett. **81**, 2735 (1998).
[5] M. V. R. Murty, T. Curcic, A. Judy, B. H. Cooper, A. R. Woll, J. D. Brock, S. Kycia, and R. L. Headrick, Phys. Rev. Lett. **80**, 4713 (1998).
[6] T. Michely and G. Comsa, Nucl. Instrum. Methods Phys. Res. B **82**, 207 (1993).
[7] S. J. Chey, J. E. van Nostrand, and D. G. Cahill, Phys. Rev. B **52**, 16 696 (1995).
[8] M. V. R. Murty, B. Cowles, and B. H. Cooper, Surf. Sci. **415**, 328 (1998).
[9] A.-L. Barabasi and H. E. Stanley, in *Fractal Concepts in Surface Growth* (Cambridge University Press, Cambridge, 1995).
[10] S. S. P. Parkin, Z. G. Li, and K. J. Smith, Appl. Phys. Lett. **58**, 2710 (1991).
[11] G. Rosenfeld, B. Poelsema, and G. Comsa, in *Growth and Properties of Ultrathin Epitaxial Layers*, edited by D. A. King and D. P. Woodruff, The Chemical Physics of Solid Surfaces (Elsevier, Amsterdam, 1997), Vol. 8, Chap. 3.
[12] R. Kunkel, B. Poelsema, L. K. Verheij, and G. Comsa, Phys. Rev. Lett. **65**, 733 (1990).
[13] M. Kalff, G. Comsa, and T. Michely, Phys. Rev. Lett. **81**, 1255 (1998).
[14] T. Michely, M. Hohage, S. Esch, and G. Comsa, Surf. Sci. Lett. **349**, L89 (1996).
[15] C. A. Lang, M. M. Dovek, J. Nogami, and C. F. Quate, Surf. Sci. Lett. **224**, L947 (1989).
[16] Y. Li and A. E. DePristo, Surf. Sci. **351**, 189 (1996).
[17] M. Siegert and M. Plishcke, Phys. Rev. Lett. **73**, 1517 (1994).
[18] R. L. Headrick, S. Kycia, Y. K. Park, A. R. Woll, and J. D. Brock, Phys. Rev. B **54**, 14 686 (1996).
[19] J. Perdereau, J. P. Biberian, and G. E. Rhead, J. Phys. F: **4**, 798 (1974).
[20] U. Harten, A. M. Lahee, J. P. Toennies, and Ch. Woll, Phys. Rev. Lett. **54**, 2619 (1985).
[21] Ch. Woll, S. Chiang, R. J. Wilson, and P. H. Lippel, Phys. Rev. B **39**, 7988 (1989).
[22] J. V. Barth, H. Brune, G. Ertl, and R. J. Behm, Phys. Rev. B **42**, 9307 (1990).
[23] A. R. Sandy, S. G. J. Mochrie, D. M. Zehner, K. G. Huang, and D. Gibbs, Phys. Rev. B **43**, 4667 (1991).
[24] The position $(0\ 0\ 1.44)_{hex}$ was chosen to reduce the contribution from the second harmonic ($\lambda=0.062$ nm) in the incident beam (which was passed by the W/B_4C multilayer monochromator).
[25] The herringbone pattern on Au(111) causes small changes in the spacings between layers near the surface and an increase in the atomic density in the top layer (Refs. 20, 21). Changes in the surface reconstruction during ion irradiation and homoepitaxy do not affect the qualitative conclusions drawn from the specular beam intensity measurements in Secs. IV and V. For the transverse x-ray scans through the $(0\ 0\ 0.15)_{hex}$ position reported in Secs. VI and VII, the influence of the reconstruction on the intensity is less than 1%.
[26] P. Bedrossian, J. E. Houston, J. Y. Tsao, E. Chason, and S. T. Picraux, Phys. Rev. Lett. **67**, 124 (1991).
[27] P. Bedrossian and T. Klitsner, Phys. Rev. B **44**, 13 783 (1991).
[28] B. Poelsema, L. K. Verheij, and G. Comsa, Phys. Rev. Lett. **53**, 2500 (1984).
[29] T. Michely, K. H. Besocke, and G. Comsa, Surf. Sci. Lett. **230**, L135 (1990).
[30] K. P. Reimann, A. Rehmet, W. Bolse, and U. Geyer, Mater. Res. Soc. Symp. Proc. **439**, 361 (1997).
[31] The coverage of layers 0 (substrate), 1 and 2 after deposition of ≈1 ML in Ref. 15 indicate that the specular beam intensity at the anti-Bragg position after 1-ML deposition should be about 30–40% of the starting value.
[32] G. Rosenfeld, N. N. Lipkin, W. Wulfhekel, J. Kliewer, K. Morgenstern, B. Poelsema, and G. Comsa, Appl. Phys. A: Solids Surf. **61**, 455 (1991).
[33] J. Tersoff, A. W. D. van der Gon, and R. M. Tromp, Phys. Rev. Lett. **72**, 266 (1994).

[34] J. Villain, J. Phys. I **1**, 19 (1991).
[35] J. G. Amar and F. Family, Phys. Rev. Lett. **77**, 4584 (1996).
[36] M. V. R. Murty and B. H. Cooper (to be published).
[37] M. D. Johnson, C. Orme, A. W. Hunt, D. Graff, J. Sudijono, L. M. Sander, and B. G. Orr, Phys. Rev. Lett. **72**, 116 (1994).
[38] J. A. Stroscio, D. T. Pierce, M. D. Stiles, A. Zangwill, and L. M. Sander, Phys. Rev. Lett. **75**, 4246 (1995).
[39] H.-J. Ernst, F. Fabre, R. Folkerts, and J. Lapujoulade, Phys. Rev. Lett. **72**, 112 (1994).
[40] J.-K. Zuo and J. F. Wendelken, Phys. Rev. Lett. **78**, 2791 (1997).
[41] M. Plischke and B. Bergersen, *Equilibrium Statistical Physics* (Prentice Hall, NJ, 1989), Chap. 4.
[42] H. You, K. G. Huang, and R. T. Kampwirth, Physica B **221**, 77 (1996).
[43] Y.-P. Zhao, H.-N. Yang, G.-C. Wang, and T.-M. Lu, Phys. Rev. B **57**, 1922 (1998).